electronics

Article

A Novel UAV-to-Multi-USV Channel Model Incorporating Massive MIMO for 6G Maritime Communications

Yuyang Zhang [1], Yi Zhang [1], Jia Liu [1], Borui Huang [1], Hengtai Chang [2], Yu Liu [1,3,*] and Jie Huang [3,4]

[1] School of Integrated Circuits, Shandong University, Jinan 250101, China; 202200400179@mail.sdu.edu.cn (Y.Z.); 202332392@mail.sdu.edu.cn (Y.Z.); 202432380@mail.sdu.edu.cn (J.L.); 202200400073@mail.sdu.edu.cn (B.H.)
[2] School of Information Science and Engineering, Shandong University, Qingdao 266237, China; changht@sdu.edu.cn
[3] National Mobile Communications Research Laboratory, School of Information Science and Engineering, Southeast University, Nanjing 211189, China; j_huang@seu.edu.cn
[4] Purple Mountain Laboratories, Nanjing 211111, China
* Correspondence: yuliu@sdu.edu.cn

Abstract

With the advancement of sixth-generation (6G) wireless communication technology, new demands have been placed on maritime communications. In maritime environments, factors such as evaporation ducts and sea waves significantly impact signal transmission. Moreover, in multi-user communication scenarios, interactions between different users introduce additional complexities. This paper proposes a novel channel model for maritime unmanned aerial vehicle (UAV) to multi-unmanned surface vehicle (USV) communications, which incorporates massive multiple-input–multiple-output (MIMO) antennas at both the transmitter (Tx) and receiver (Rx), while also accounting for the effects of evaporation ducts and sea waves on the channel. For the USV-single-user maritime model, the temporal auto-correlation function (ACF) and spatial cross-correlation function (CCF) are analyzed. For the UAV-to-multi-user channel model, key channel characteristics such as channel matrix collinearity (CMC) and channel capacity are examined. Finally, the accuracy and effectiveness of the proposed model are validated through a comparison between the measured and simulated data under a single-link environment. Meanwhile, a comparison between the CMC obtained from the proposed model and that derived from Ray-Tracing further verifies the model's accuracy in multi-link environments. This model provides essential theoretical guidance for future 6G maritime communication systems.

Keywords: channel modeling; UAV-to-multi-USV channels; channel characteristics; massive MIMO; channel correlation

check for updates

Academic Editor: Dimitra I. Kaklamani

Received: 28 April 2025
Revised: 17 June 2025
Accepted: 17 June 2025
Published: 23 June 2025

Citation: Zhang, Y.; Zhang, Y.; Liu, J.; Huang, B.; Chang, H.; Liu, Y.; Huang, J. A Novel UAV-to-Multi-USV Channel Model Incorporating Massive MIMO for 6G Maritime Communications. *Electronics* **2025**, *14*, 2536. https:// doi.org/10.3390/electronics14132536

Copyright: © 2025 by the authors. Licensee MDPI, Basel, Switzerland. This article is an open access article distributed under the terms and conditions of the Creative Commons Attribution (CC BY) license (https://creativecommons.org/licenses/by/4.0/).

1. Introduction

With the rapid development of sixth-generation (6G) communication technologies and the growing demand for maritime network connectivity, unmanned aerial vehicles (UAVs) play an indispensable part in maritime communication systems [1,2]. As a pivotal airborne node of 6G maritime communication, UAVs offer highly timely and efficient solutions for applications such as maritime search and rescue. However, signal propagation in maritime environments is easily affected by complex factors such as ocean surface fluctuations and evaporation ducts. These factors bring unique maritime UAV channel characteristics, which are distinguished from traditional terrestrial channels [3]. Additionally, maritime communication systems often require multiple terminal devices to simultaneously receive signals

from a single transmitter (Tx). For example, in scenarios like ocean transportation [4], multiple unmanned surface vehicles (USVs) need to communicate and coordinate with a single UAV. To enhance system capacity through spatial multiplexing, both the UAV and multiple USVs are typically equipped with massive multiple-input–multiple-output (MIMO) antennas [5,6]. Among the different USV receivers (Rxs), there exists channel correlation which significantly impacts the overall performance of the maritime communication system. Therefore, investigating channel modeling in multi-user scenarios is essential for enhancing the stability and reliability of maritime UAV communication systems.

Currently, based on existing channel models, researchers have conducted lots of studies on various channel characterizations in maritime scenarios. Many broadband maritime channel measurements were taken in [7–13]. In [7], the results showed that ocean waves influence ship movement, affecting the Doppler shift of the line-of-sight (LoS) path. Building on this, in [8], channel characteristics such as the Rician K-factor and coherence bandwidth exhibited rapid changes within a short time, indicating a high degree of non-stationarity in maritime communication channels. Moreover, it was found that the primary factor affecting root mean square (RMS) delay spread (DS) is the distance between the Tx and Rx [9]. In [10], the oceanic power delay profile (PDP) exhibited a sharp peak shape due to isolated scattering in the environment. Based on these non-stationary characteristics of the channel, in [11], the authors investigated X-band communication for maritime applications in the South China Sea. Analysis of the results revealed that optimal transmission conditions can be achieved within the 8–12 GHz frequency range. Additionally, propagation distance is a crucial parameter that influences channel characteristics. Different propagation distances require different modeling and calculation methods. In [12], the authors conducted radio propagation measurements between a UAV and a base station on a sailing vessel. Analysis of the results revealed that for short and long propagation distances, the channel can be modeled using the log-distance model and the two-ray model, respectively. In [13], the authors proposed a stochastic ray-tracing approach for maritime multipath channel modeling. The outage probability of the channel was investigated with key parameters such as the number of diffuse reflection paths.

With the advancement of technology, UAV-based multi-user communication channel models are being utilized in an increasing number of scenarios. In [14], the authors proposed an ultra-massive MIMO beam domain channel model (BDCM) for 6G maritime communications. The accuracy of the model was validated through comparisons between simulation results and measured RMS DS data. In [15], a three-dimensional (3D) non-stationary MIMO geometry-based stochastic model (GBSM) for ship-to-ship maritime communication channels was proposed. This model accounts for the movement of the Tx and Rx, environmental variations and the MIMO antenna array, effectively reflecting the spatiotemporal non-stationary characteristics of the channel. Additionally, in maritime communication systems, the cooperative operation between the UAV and multiple USVs is a future development trend [16]; many researchers have studied various channel parameters of multi-user channel models. In [17], the study demonstrated that UAV height, user density, and antenna layouts significantly impact inter-user channel correlation and channel capacity. In [18], the authors proposed a maritime multi-user MIMO communication channel model. Through result analysis, it was found that the correlation between multi-user channels increases as the distance between the Tx and Rx increases. In [19], the authors analyzed a multi-user massive MIMO system for maritime terminals in a multi-cell environment and derived a mathematical formula for the outage probability using maximum ratio transmission precoding.

Existing studies have effectively modeled and analyzed the communication channel between UAVs and USVs in maritime environments. However, several important issues

remain to be addressed. For instance, current research on maritime communication channel models primarily focuses on the channel between a UAV and a single USV, which lacks an analysis of the inter-channel relationships among multiple USVs, especially the analysis of how different factors affect the correlation between the different channels. In addition, the MIMO channel is always assumed to be an independent and identically distributed Gaussian random process with zero mean and unit variance in traditional models [20,21]. Such modeling is suitable for static mathematical analysis but neglects the spatial correlation between antennas and the physical geometry of the array. In contrast, in UAV-to-multi-USV scenarios, multiple USVs are distributed over the sea surface, forming a distributed and dynamically evolving MIMO array. The channel characteristics in this case strongly depend on the antenna array configuration, sea surface reflections and other complex factors.

This study aims to propose a novel UAV-to-multi-USV channel model for maritime communications. In the model, both the UAV and multiple USVs are equipped with MIMO antennas. Additionally, the proposed channel model incorporates the birth–death process of clusters to simulate the observability of clusters in complex environments. During channel characteristic analysis such as channel correlation, a simplified UAV-to-multi-USV model is adopted, where mutual interference between USVs is neglected to facilitate the study of inter-channel correlation. In contrast, the subsequent channel capacity analysis incorporates inter-USV interference by introducing the inter-link interference covariance matrix R_I to characterize its impact. The main contributions of this study are as follows:

1. A novel UAV-to-multi-USV channel model for maritime communication is proposed. This model involves multiple communication links between the UAV and multiple USVs, focusing on analyzing the relationship between different communication links among USVs. Moreover, the antenna configurations at both the transmitting and receiving ends adopt massive MIMO.
2. The P-M wave spectrum model is used to generate a 3D representation of the sea surface under a given wind speed, and the evaporation duct angle formula is applied to calculate the impact of the evaporation duct on cluster angles. Furthermore, the maritime environment parameters are also incorporated into the proposed model to accurately mimic real signal propagation.
3. Based on the proposed model, the impact of UAV flight height, wind speed, and the number of antennas on the channel matrix collinearity (CMC) is investigated, and channel capacity of multiple USVs is compared. Additionally, some typical statistical properties of the channel model, such as the temporal auto-correlation function (ACF) and spatial cross-correlation function (CCF), are presented by considering the effects of frequency bands, Tx antenna orientations, and antenna array layouts. Finally, the observability of clusters is visually presented.

The rest of this paper is organized as follows. In Section 2, a UAV-to-multi-USV maritime communication model is proposed. In Section 3, typical statistical properties of the novel channel model are studied. Results and analysis are provided in Section 4. Model comparison and analysis are provided in Section 5. Conclusions are drawn in Section 6.

2. A Novel Channel Model for Maritime UAV-to-Multi-USV Communications

2.1. Channel Model Framework Construction

The network architecture of the proposed novel maritime UAV-to-multi-USV communication channel model is illustrated in Figure 1. In Figure 1, the left side represents the UAV, while the right side depicts the multiple USVs. The yellow, green, and purple lines represent different communication channels between the UAV and each USV. In the UAV-to-single-USV communication channel, both LoS and non-line-of-sight (NLoS) paths

exist. In the analysis, the NLoS path is typically decomposed into path N1 and path N2. The two paths represent virtual paths formed by evaporation duct clusters and sea surface clusters, respectively. These paths are generated independently.

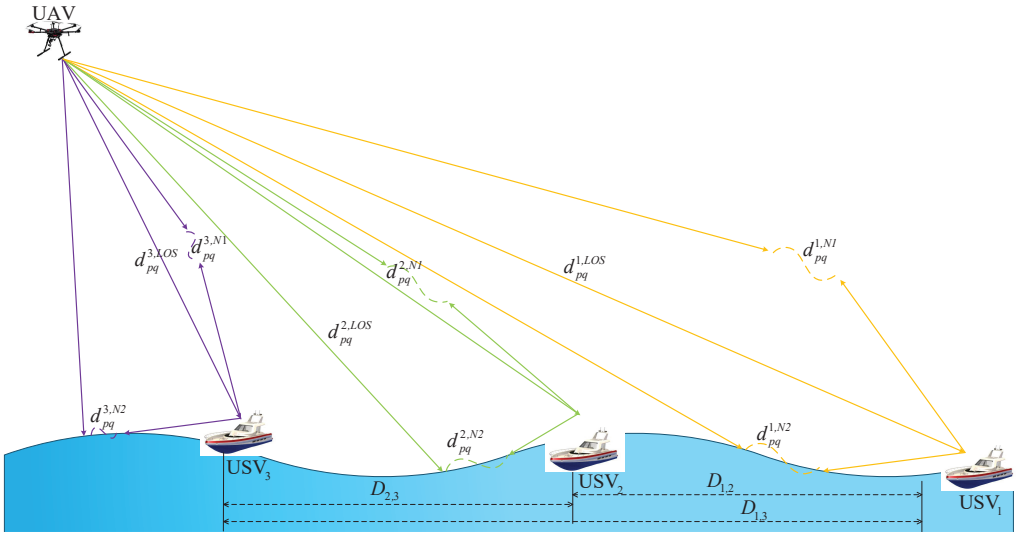

Figure 1. Network architecture of the maritime UAV-to-multi-USV communications.

Figure 2 introduces the construction of the channel model for a single-link channel. In Figure 2, the transmitting antenna emits signals, with one part reaching the receiving antenna directly via the LoS path, while the other part arrives via the NLoS path. Along the NLoS path, the signal undergoes an initial reflection by the first scatterer cluster $C_{N1/N2}^{i,A}$ and a final reflection by the last scatterer cluster $C_{N1/N2}^{i,Z}$. Additionally, $l_{C_{N1/N2}}^{i,A}$ and $l_{C_{N1/N2}}^{i,Z}$ are the path points within the clusters $C_{N1/N2}^{i,A}$ and $C_{N1/N2}^{i,Z}$. In addition, due to the uncertainty of the maritime environment, the value of $C_{N1/N2}^{i,pq}(t)$ and $l_{C_{N1/N2}}^{i,pq}(t)$ are modeled as Poisson-distributed random variables at the corresponding moment. In Figure 2, red circles and light blue circles represent the centers of clusters $C_{N1}^{i,A}$ and $C_{N2}^{i,Z}$, while the outer ellipsoids represent the distribution range of path points within clusters. For the LoS path between A_p^T and $A_q^{i,R}$, the real-time azimuth angle of departure (AAoD), the elevation angle of departure (EAoD), the azimuth angle of arrival (AAoA), and the elevation angle of arrival (EAoA) as well as the distance are denoted as $\alpha_{A,LoS}^{i,T,p}$, $\alpha_{E,LoS}^{i,T,p}$, $\alpha_{A,LoS}^{i,R,q}$, $\alpha_{E,LoS}^{i,R,q}$ and $d_{pq}^{i,LOS}$. For the deployment of multiple antennas, we adopted two configurations: the uniform linear array (ULA) and the uniform circular array (UCA). In the correlation analysis, we focused on investigating the impact of factors such as wind speed and UAV altitude on channel correlation, while simplifying the treatment of the number of antennas. For example, the number of ULA antenna was set as 1×2 . When studying the effect of antenna count on correlation, we set the number of antennas to 2, 9, and 64, respectively. The antenna spacing was set to half a wavelength, and the elevation angles of the antennas mounted on the UAV and USV were both set to 45°. Other parameters used in the model are summarized in Table 1.

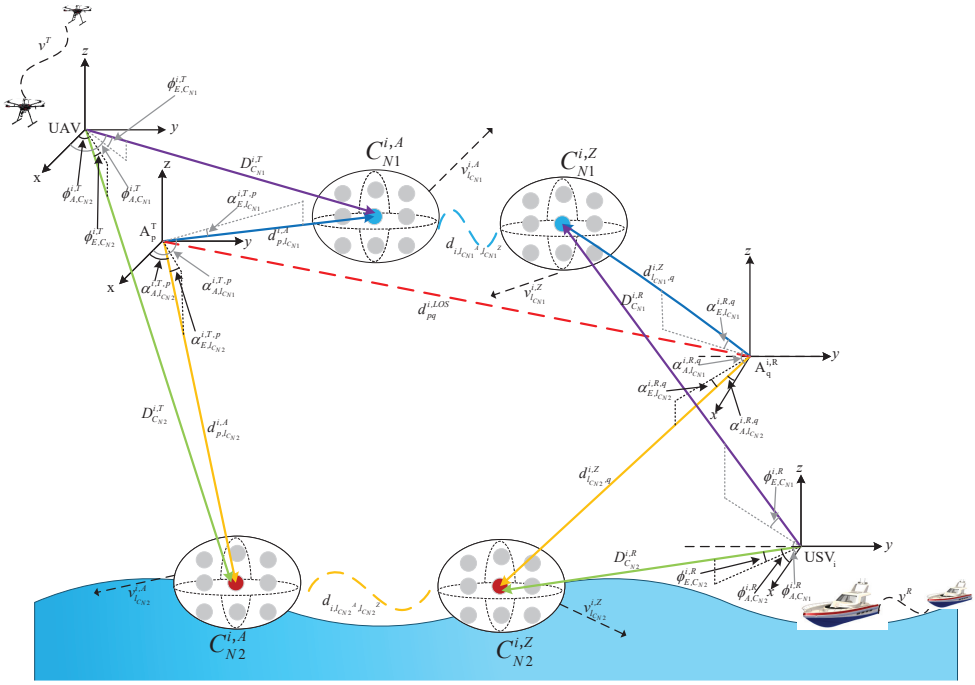

Figure 2. Architecture diagram of the maritime UAV-to-single-USV channel model.

Table 1. Definition of parameters.

Parameters	Definition
A^T, $A^{i,R}$	Coordinates of the UAV and USV
A_p^T, $A_q^{i,R}$	Coordinates of the transmitting antenna p and receiving antenna q
$C_{N1}^{i,pq}(t)$, $C_{N2}^{i,pq}(t)$	Number of evaporation duct clusters/sea surface clusters between A_p^T and $A_q^{i,R}$
$l_{C_{N1}}^{i,pq}(t)$, $l_{C_{N2}}^{i,pq}(t)$	Number of path points in $C_{N1}^{i,pq}(t)$ and $C_{N2}^{i,pq}(t)$
v^T, $v^{i,R}$, $v_{C_{N1/N2}}^{i,A/Z}$	Velocity of the UAV, USV, and cluster $C_{N1/N2}^{i}$
$D_{C_{N1/N2}}^{i,T}$, $D_{C_{N1/N2}}^{i,R}$	Distance from A^T and $A^{i,R}$ to the clusters $C_{N1/N2}^{i,A}$ and $C_{N1/N2}^{i,Z}$
$\alpha_{A,l_{C_{N1/N2}}}^{i,T,p}$, $\alpha_{E,l_{C_{N1/N2}}}^{i,T,p}$	AAOD and EAOD from A_p^T to cluster $C_{N1/N2}^{i,A}$
$\alpha_{A,l_{C_{N1/N2}}}^{i,R,q}$, $\alpha_{E,l_{C_{N1/N2}}}^{i,R,q}$	AAOA and EAOA from $A_q^{i,R}$ to cluster $C_{N1/N2}^{i,Z}$
$\beta_{A,C_{N1/N2}}^{i,A/Z}$, $\beta_{E,C_{N1/N2}}^{i,A/Z}$	Azimuth angle and elevation angle of the movement of clusters $C_{N1/N2}^{i,A}$ and $C_{N1/N2}^{i,Z}$

2.2. Description of the Maritime UAV-Multi-USV Channel Model

For the maritime UAV-to-multi-USV channel model, the total number of USVs is denoted as M and the total channel matrix $\mathbf{H}$ is expressed as

$$\mathbf{H} = \sum_{i=1}^{M} \mathbf{H}_i \tag{1}$$

where $\mathbf{H}_i$ is the channel matrix from the UAV to the i-th USV, and $\mathbf{H}_i$ is given as follows:

$$\mathbf{H}_i = [PL_i \cdot SH_i]^{1/2} \cdot \mathbf{H}_{si} \tag{2}$$

where PL_i, SH_i and $\mathbf{H}_{si}$ represent the path loss, shadow fading and total impulse response of the channel from the UAV to the i-th USV. $\mathbf{H}_{si}$ is a $M_T \times M_R$ matrix, in which $h^i_{pq}(t,\tau)$ denotes the impulse response of the channel between A^T_p and $A^{i,R}_q$. K_r is the Rician K-factor, and α_1 and α_2 are the power correlation coefficients of two path components. The expressions for $\mathbf{H}_{si}$ and $h^i_{pq}(t,\tau)$ are given by

$$\mathbf{H}_{si} = [h^i_{pq}(t,\tau)]_{M_T \times M_R} \tag{3}$$

$$\begin{aligned} h^i_{pq}(t,\tau) =& \sqrt{\frac{K_r}{K_r+1}} h^{i,pq}_{LoS}(t) \cdot \delta\left(\tau - \tau^{i,pq}_{LoS}(t)\right) + \sqrt{\frac{\alpha_1}{K_r+1}} h^{i,pq}_{l_{C_{N1}}}(t) \cdot \delta\left(\tau - \tau^{i,pq}_{l_{C_{N1}}}(t)\right) \\ &+ \sqrt{\frac{\alpha_2}{K_r+1}} h^{i,pq}_{l_{C_{N2}}}(t) \cdot \delta\left(\tau - \tau^{i,pq}_{l_{C_{N2}}}(t)\right) \end{aligned} \tag{4}$$

the expressions of $h^{i,pq}_{LoS}(t,\tau)$, $h^{i,pq}_{l_{C_{N1}}}(t)$ and $h^{i,pq}_{l_{C_{N2}}}(t)$ are given as follows:

$$\begin{aligned} h^{i,pq}_{LoS}(t) =& \begin{bmatrix} F_{q,V}\left(\alpha^{i,R,q}_{E,LoS}, \alpha^{i,R,q}_{A,LoS}\right) \\ F_{q,H}\left(\alpha^{i,R,q}_{E,LoS}, \alpha^{i,R,q}_{A,LoS}\right) \end{bmatrix}^T \begin{bmatrix} e^{j\Theta^{i,VV}_{LoS}} & 0 \\ 0 & e^{j\Theta^{i,HH}_{LoS}} \end{bmatrix} \begin{bmatrix} F_{p,V}\left(\alpha^{i,T,p}_{E,LoS}, \alpha^{i,T,p}_{A,LoS}\right) \\ F_{p,H}\left(\alpha^{i,T,p}_{E,LoS}, \alpha^{i,T,p}_{A,LoS}\right) \end{bmatrix} \\ &\times e^{j2\pi f_c \tau^{i,pq}_{LoS}(t)} \end{aligned} \tag{5}$$

$$\begin{aligned} h^{i,pq}_{l_{C_X}}(t) =& \sum_{C^i_X=1}^{C^{i,pq}_X(t)} \sum_{l^i_{C_X}=1}^{l^{i,pq}_{C_X}(t)} \begin{bmatrix} F_{q,V}\left(\alpha^{i,R,q}_{E,l_{C_X}}, \alpha^{i,R,q}_{A,l_{C_X}}\right) \\ F_{q,H}\left(\alpha^{i,R,q}_{E,l_{C_X}}, \alpha^{i,R,q}_{A,l_{C_X}}\right) \end{bmatrix}^T \begin{bmatrix} e^{j\Theta^{i,VV}_{l_{C_X}}} & \sqrt{\kappa^{-1}_{l_{C_X}}} e^{j\Theta^{i,VH}_{l_{C_X}}} \\ \sqrt{\kappa^{-1}_{l_{C_X}}} e^{j\Theta^{i,HV}_{l_{C_X}}} & e^{j\Theta^{i,HH}_{l_{C_X}}} \end{bmatrix} \\ &\cdot \begin{bmatrix} F_{p,V}\left(\alpha^{i,T,p}_{E,l_{C_X}}, \alpha^{i,T,p}_{A,l_{C_X}}\right) \\ F_{p,H}\left(\alpha^{i,T,p}_{E,l_{C_X}}, \alpha^{i,T,p}_{A,l_{C_X}}\right) \end{bmatrix} \sqrt{P^{i,pq}_{l_{C_X}}(t)} \times e^{j2\pi f_c \tau^{i,pq}_{l_{C_X}}(t)} \cdot \mathbf{B}^i_{p,q,C_X} \end{aligned} \tag{6}$$

where $X \in \{N1/N2\}$, $[\cdot]^T$ denotes the transpose operation, f_c represents the carrier frequency. $F_{p/q,V}$ and $F_{p/q,H}$ denote the directional patterns of horizontal and vertical polarization antennas at the UAV and USV. And $l^i_{C_{N1/N2}}$ refers to the path point within the cluster $C^i_{N1/N2}$. $\kappa_{l_{C_{N1/N2}}}$ represents the cross-polarization power ratio of the path $N1/N2$, $\Theta^{i,VV}_{LoS}$, $\Theta^{i,HH}_{LoS}$, $\Theta^{i,VV}_{l_{C_{N1/N2}}}$, $\Theta^{i,VH}_{l_{C_{N1/N2}}}$, $\Theta^{i,HV}_{l_{C_{N1/N2}}}$ and $\Theta^{i,HH}_{l_{C_{N1/N2}}}$ are initial phases uniformly distributed according to $(0, 2\pi)$. $P^{i,pq}_{l_{C_{N1/N2}}}(t)$ represents the power of the path passing through path point $l^i_{C_{N1/N2}}$ at time t. $\tau^{i,pq}_{LoS}(t)$ and $\tau^{i,pq}_{l_{C_{N1/N2}}}(t)$ represent the signal delay for the corresponding paths. Finally, $\mathbf{B}^i_{p,q,C_{N1/N2}}$ represents the cluster birth–death process matrix. It indicates whether the cluster can be observed by the transmitting and receiving antennas.

2.2.1. Calculation of the Height of the USV

In common communication scenarios, the Rx is typically in a state of slow movement. However, the situation differs when the UAV communicates with USVs in maritime scenarios. Due to the wind at the sea surface, the height of the USV fluctuates in real time because of the ocean waves. The amplitude and rate of change of the height are closely related to the wind speed. The calculation method for the height of the USV $A^{i,R}_z$ is as follows [15]:

$$A^{i,R}_z = \sum_{m=1}^{K} a_m \cos[\omega_m t + \epsilon_m] \tag{7}$$

where K represents the number of composite waves, and ω_m, a_m and ϵ_m represent the angular frequency, amplitude and random initial phase of the m-th wave. a_m is given by the following equation:

$$a_m = 2\sqrt{S(\omega_m)}\Delta\omega\Delta\varphi \tag{8}$$

where $\Delta\omega$ is the frequency interval between different waves, and $\Delta\varphi$ is the angular interval between different waves. $S(\omega_m)$ denotes the wave spectrum of the m-th composite wave, which is described using the Pierson–Moskowitz (P-M) spectrum as follows:

$$S(\omega) = \frac{p_1 g^2}{\omega^5}\exp\left[-\frac{p_2}{U\omega}\right]^4 \tag{9}$$

where $p_1 = 8.1 \times 10^{-3}$ and $p_2 = 0.74$ are dimensionless constants, and U is the wind speed at 19.5 m above the sea surface.

2.2.2. Generation and Evolution of Small-Scale Parameters

Let $M_{C_{N1/N2}}^{i,A/Z}$ denote the coordinates of cluster $C_{N1/N2}^{i,A/Z}$ when the UAV communicates with the i-th USV. It can be derived from the evolution of ${}^{[0]}M_{C_{N1/N2}}^{i,A/Z}$:

$$M_{C_{N1/N2}}^{i,A/Z}(t) = {}^{[0]}M_{C_{N1/N2}}^{i,A/Z} + v_{C_{N1/N2}}^{i,A/Z}(t-t_0)\cdot\begin{bmatrix}\cos\beta_{A,C_{N1/N2}}^{i,A/Z}\cdot\cos\beta_{E,C_{N1/N2}}^{i,A/Z}\\ \sin\beta_{A,C_{N1/N2}}^{i,A/Z}\cdot\cos\beta_{E,C_{N1/N2}}^{i,A/Z}\\ \sin\beta_{E,C_{N1/N2}}^{i,A/Z}\end{bmatrix}^T \tag{10}$$

where $v_{C_{N1/N2}}^{i,A/Z} \sim \mathcal{N}(0,\sigma_w^2)$ and $\beta_{A/E,C_{N1/N2}}^{i,A/Z} \sim \mathcal{U}(0,2\pi)$. They indicate that the cluster movement exhibits randomness in both speed and direction. And the parameter σ_w represents the noise intensity, which directly determines the magnitude of velocity fluctuations in cluster movement. ${}^{[0]}M_{C_{N1/N2}}^{i,A/Z}$ denotes the coordinates of cluster $C_{N1/N2}^{i,A/Z}$ at the initial moment t_0. Its expression is given as follows:

$${}^{[0]}M_{C_{N1/N2}}^{i,A} = {}^{[0]}A^T + D_{C_{N1/N2}}^{i,T}\cdot\begin{bmatrix}\cos\Phi_{A,C_{N1/N2}}^{i,T}\cos\Phi_{E,C_{N1/N2}}^{i,T}\\ \sin\Phi_{A,C_{N1/N2}}^{i,T}\cos\Phi_{E,C_{N1/N2}}^{i,T}\\ \sin\Phi_{E,C_{N1/N2}}^{i,T}\end{bmatrix} \tag{11}$$

$${}^{[0]}M_{C_{N1/N2}}^{i,Z} = {}^{[0]}A^{i,R} + D_{C_{N1/N2}}^{i,R}\cdot\begin{bmatrix}\cos\Phi_{A,C_{N1/N2}}^{i,R}\cos\Phi_{E,C_{N1/N2}}^{i,R}\\ \sin\Phi_{A,C_{N1/N2}}^{i,R}\cos\Phi_{E,C_{N1/N2}}^{i,R}\\ \sin\Phi_{E,C_{N1/N2}}^{i,R}\end{bmatrix}. \tag{12}$$

At the initial moment, $D_{C_{N1/N2}}^{i,T}$ is the distance from ${}^{[0]}A^T$ to the cluster $C_{N1/N2}^{i,A}$, and $D_{C_{N1/N2}}^{i,R}$ is the distance from ${}^{[0]}A^{i,R}$ to the cluster $C_{N1/N2}^{i,Z}$. $\Phi_{A,C_{N1/N2}}^{i,T}$, $\Phi_{E,C_{N1/N2}}^{i,T}$, $\Phi_{A,C_{N1/N2}}^{i,R}$ and $\Phi_{E,C_{N1/N2}}^{i,R}$ represent the AAOD and EAOD of the cluster $C_{N1/N2}^{i,A}$ and the AAOA and EAOA of the cluster $C_{N1/N2}^{i,Z}$. Their calculation method is given as follows:

The cluster angle $\Phi_{A/E,C_{N1/N2}}^{i,T/R}$ follows a normal distribution. Its upper and lower bounds a and b are related to $\theta_{limit}^{i,T/R}$ [15]. $\theta_{limit}^{i,T/R}$ denotes the capture angle of the cluster. It represents the upper and lower limits of the cluster angle. The formulas are given by

$$f(\Phi) = \frac{\frac{1}{\sigma_\Phi\sqrt{2\pi}}\exp\left(\frac{-(\Phi-\mu_\Phi)}{2\sigma_\Phi^2}\right)}{F\left(\frac{a-\mu_\Phi}{\Phi}\right)-F\left(\frac{b-\mu_\Phi}{\sigma_\Phi}\right)} \tag{13}$$

$$\theta_{limit}^{i,T/R} = \sqrt{2(\frac{1}{n(0)}\frac{dn(z)}{dz}\Big|_{z=h_d} + \frac{1}{R_e})(^{[0]}A^{T/i,R} - h_d)} \tag{14}$$

where $n(z)$ represents the refractive index, $n(0)$ is the refractive index at sea level, R_e is the Earth's radius and h_d is the height of the oceanic duct. $\frac{dn(z)}{dz}$ represents the vertical gradient of the refractive index, which can be obtained from the following equation:

$$\frac{dn(z)}{dz} = \left(\frac{dM(z)}{dz} - 0.157\right) \times 10^{-6} \tag{15}$$

where $M(z)$ is the modified refractive index. The expression is given by the equation

$$M(z) = M_0 + 0.125z - 0.125h_d \ln\left(\frac{z + z_0}{z_0}\right). \tag{16}$$

Moreover, since the sea surface cluster $C_{N2}^{i,A}$ is fixed on the sea surface, let $h_{^{[0]}A^T}$ denote the height of the UAV relative to the cluster $C_{N2}^{i,A}$. The calculation formula of $D_{C_{N2}}^{i,T}$ is given as follows:

$$D_{C_{N2}}^{i,T} = h_{^{[0]}A^T} / \cos\left(\frac{\pi}{2} - \theta_{limit}^{i,T}\right). \tag{17}$$

Based on the above analysis, the positions of path points within the cluster can be determined. Let the coordinates of $l_{C_{N1/N2}}^{i,A/Z}$ be defined as $L_{C_{N1/N2}}^{i,A/Z}$. $L_{C_{N1/N2}}^{i,A/Z}$ follows a three-dimensional Gaussian distribution with respect to $M_{C_{N1/N2}}^{i,A/Z}$ and is determined by the following equation:

$$L_{C_{N1/N2},x}^{i,A/Z} = M_{C_{N1/N2},x}^{i,A/Z} + \Delta x_{l_{C_{N1/N2}}}^{i,A/Z} \tag{18}$$

$$L_{C_{N1/N2},y}^{i,A/Z} = M_{C_{N1/N2},y}^{i,A/Z} + \Delta y_{l_{C_{N1/N2}}}^{i,A/Z} \tag{19}$$

$$L_{C_{N1/N2},z}^{i,A/Z} = M_{C_{N1/N2},z}^{i,A/Z} + \Delta z_{l_{C_{N1/N2}}}^{i,A/Z}. \tag{20}$$

2.2.3. The Calculation of Cluster Birth–Death Process Matrix

In practical communication, some clusters may not be observed due to the complex environmental factors. Therefore, the cluster birth–death matrix $\mathbf{B}_{p,q,C_{N1/N2}}^{i}$ is introduced, which is expressed as follows:

$$\begin{aligned}\mathbf{B}_{p,q,C_{N1/N2}}^{i} = &\left(\left\|\overrightarrow{A}_p^T - \overrightarrow{B}_{C_{N1/N2}}^{i,T}\right\|_F < L^T\left(C_{N1/N2}^{i}\right)\right) \\ &\cdot \left(\left\|\overrightarrow{A}_q^{i,R} - \overrightarrow{B}_{C_{N1/N2}}^{i,R}\right\|_F < L^R\left(C_{N1/N2}^{i}\right)\right)\end{aligned} \tag{21}$$

where $\overrightarrow{B}_{C_{N1/N2}}^{i,T}$ and $\overrightarrow{B}_{C_{N1/N2}}^{i,R}$ represent the vectors from the origin to the centers of the observable regions of clusters $C_{N1/N2}^{i,A}$ and $C_{N1/N2}^{i,Z}$, $\overrightarrow{A}_p^T$ and $\overrightarrow{A}_q^{i,R}$ are vectors from the origin to A_p^T and $A_q^{i,R}$, and $L^T\left(C_{N1/N2}^{i}\right)$ and $L^R\left(C_{N1/N2}^{i}\right)$ denote the observable radii of the clusters $C_{N1/N2}^{i,A}$ and $C_{N1/N2}^{i,Z}$. This equation shows that a cluster is observable when the distances from the centers of the observable region to A_p^T and $A_q^{i,R}$ are smaller than observable radii. In this case, the corresponding position in matrix $\mathbf{B}_{p,q,C_{N1/N2}}^{i}$ is assigned a value of 1. For A_p^T, the observable radius $L^T\left(C_{N1/N2}^{i}\right)$ is given as follows:

$$L^T\left(C_{N1/N2}^{i}\right) = \max\left\{k\prod_{i=1}^{k}\exp\left(-\lambda_R\frac{\delta_T}{D_{cor}}\right) > U_{C_{N1/N2}^{i}}^{T}\right\}\delta_T \tag{22}$$

where λ_R is the recombination rate in the cluster evolution process, D_{cor} represents the correlation distance, δ_T denotes the spacing between antennas and $U^T_{C^i_{N1/N2}}$ follows a uniform distribution in $(0, 1)$ [17].

The overall process of channel modeling is illustrated in Figure 3 .

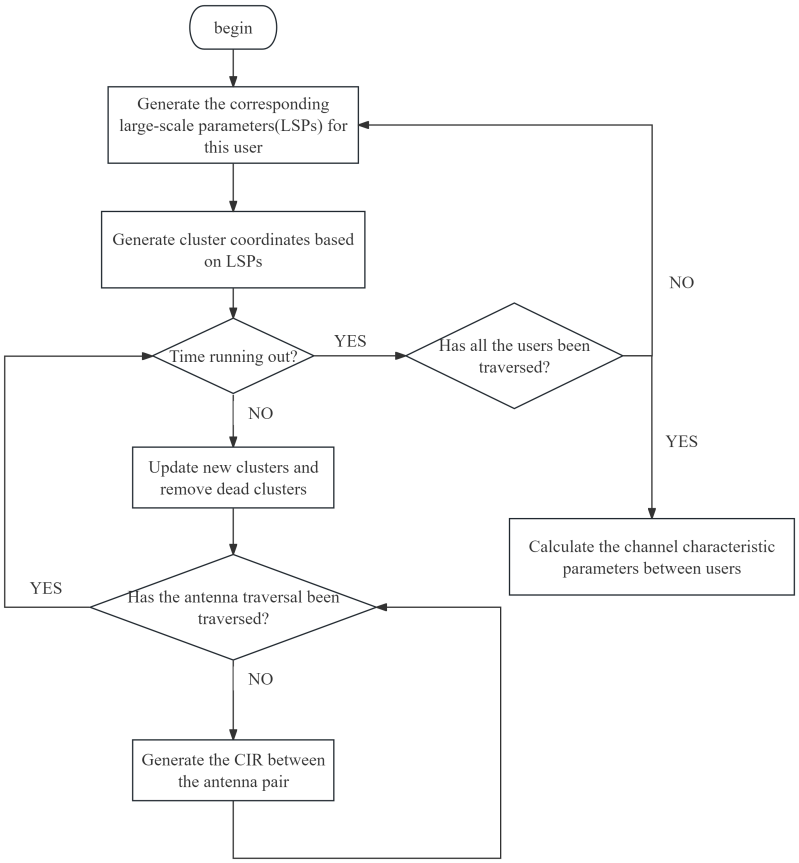

Figure 3. Flowchart of the code modeling process for the normal channel model.

3. Typical Statistical Properties of Proposed Model

3.1. CMC

The CMC serves as an index to evaluate the spatial structural variation between two matrices of the same size. It compares the subspaces of two complex matrices to quantify their similarity. In this channel model, for any two USVs $u1$ and $u2$, the CMC between the two USVs can be computed using the following equation:

$$c(u1, u2) = E\left\{ \frac{\mathrm{tr}\{\mathbf{H}^*_{u1}\mathbf{H}_{u2}\}}{\|\mathbf{H}_{u1}\|_F \|\mathbf{H}_{u2}\|_F} \right\} \tag{23}$$

where $\mathbf{H}_{u1}$ and $\mathbf{H}_{u2}$ represent the channel matrices of $u1$ and $u2$ at different carrier frequency points, and $(\cdot)^*$ denotes the conjugate operation. Finally, the overall correlation matrix C for the system is obtained:

$$C = [c(u1, u2)]_{M \times M}. \tag{24}$$

3.2. Channel Capacity

Channel capacity is the highest possible transmission rate at which information can be sent over a channel without error. It is a crucial performance metric for maritime

communication systems. For the i-th USV in a multi-USV receiving system, the channel capacity from the UAV to the i-th USV can be determined as follows:

$$C_i(t) = \log_2\left[\det\left(\mathbf{I}_{M_R\times M_R} + \frac{\rho}{M_T}[\mathbf{H}_{si}(t)]^H\mathbf{H}_{si}(t)\mathbf{R}_I{}^{-1}\right)\right] \tag{25}$$

where $(\cdot)^H$ denotes the conjugate transpose operation. $\mathbf{H}_{si}(t)$ represents the total impulse response of the channel from the UAV to the i-th USV. Additionally, $\mathbf{R}_I$ is the instantaneous covariance matrix of the inter-channel interference among multiple USVs, which is expressed as $\mathbf{R}_I = \eta\left(\mathbf{H}^I\right)^H\mathbf{H}^I + \mathbf{I}_{M_R\times M_R}$. η represents the Interference-to-Noise Ratio (INR). $\mathbf{H}^I$ is the normalized matrix of the interference links between different USVs.

3.3. STCF in a Single-Link

In maritime communication, the space–time correlation function (STCF) represents the spatial and temporal correlations of a single-link communication channel. It reflects the channel's sensitivity to temporal variations and antenna position changes, serving as a key parameter for studying the stability of maritime communication channels. $R^i_{pq}(t,\Delta t,\Delta\xi)$ represents the STCF between $h^i_{pq}(t)$ and $h^i_{p'q'}(t-\Delta t)$. Its expression is given as follows:

$$\begin{aligned} R^i_{pq}(t,\Delta t,\Delta\xi) &= E\left[h^i_{pq}(t,0,0)h^i_{pq}(t,\Delta t,\Delta\xi)\right] \\ &= \sqrt{\frac{K_r}{K_r+1}}R^{i,LoS}_{pq}(t,\Delta t,\Delta\xi) + \sqrt{\frac{\alpha_1}{K_r+1}}R^{i,N1}_{pq}(t,\Delta t,\Delta\xi) \\ &\quad + \sqrt{\frac{\alpha_2}{K_r+1}}R^{i,N2}_{pq}(t,\Delta t,\Delta\xi). \end{aligned} \tag{26}$$

Let the total virtual path length of the communication link passing through path point $l^i_{C_{N1/N2}}$ be $d^{i,pq}_{l_{C_{N1/N2}}}$. To simplify the model, the following analysis is based on a single-path model. Each component of the formula can be expressed as

$$R^{i,LoS}_{pq}(t,\Delta t,\Delta\xi) = e^{j\frac{2\pi}{\lambda}\left(\,d^{i,LoS}_{pq}(t)-d^{i,LoS}_{p'q'}(t-\Delta t)\right)} \tag{27}$$

$$R^{i,N1/N2}_{pq}(t,\Delta t,\Delta\xi) = \sum_{n=1}^{C^{i,pq}_{N1/N2}(t)} a_n\cdot e^{j\frac{2\pi}{\lambda}\left(d^{i,pq}_{l_n}(t)-d^{i,p'q'}_{l_n}(t-\Delta t)\right)} \tag{28}$$

where $a_n = \sqrt{P^{i,pq}_{l_n}(t) * P^{i,p'q'}_{l_n}(t-\Delta t)}$. By setting the spatial distance parameter $\Delta\xi = 0$, the ACF can be obtained. Similarly, by setting the temporal interval parameter $\Delta t = 0$, the CCF can be obtained.

3.4. RMS DS

The RMS DS σ_τ is defined to quantify the extent of signal dispersion in the time delay domain during transmission. It is mathematically formulated as follows:

$$\sigma_\tau = \sqrt{\overline{\eta^2} - (\overline{\eta})^2}. \tag{29}$$

Let $C^{i,pq}_X(t) = C^{i,pq}_{N1}(t) + C^{i,pq}_{N2}(t)$, $l^{i,pq}_X(t) = l^{i,pq}_{C_{N1}}(t) + l^{i,pq}_{C_{N2}}(t)$, each component of the formula can be expressed as

$$\overline{\eta^2} = \sum_{n=1}^{C^{i,pq}_X(t)}\sum_{l=1}^{l^{i,pq}_X(t)} P^{i,pq}_{n,l}(t)\left[\tau^{i,pq}_{n,l}(t)\right]^2 \tag{30}$$

$$\overline{\eta} = \sum_{n=1}^{C_X^{i,pq}(t)} \sum_{l=1}^{I_X^{i,pq}(t)} P_{n,l}^{i,pq}(t)\, \tau_{n,l}^{i,pq}(t) \tag{31}$$

4. Results and Analysis

During channel simulation initialization, the positions of USVs are generated using a Poisson distribution. The distribution is always based on the given cell radii and Rx density [17]. To better illustrate the relationship between the distance between USVs and CMC, a clear visual representation of channel characteristics is needed. Therefore, in the following simulations, all the USVs are arranged in a linear array on the sea surface, and the parameter settings for each figure are summarized in Table 2. Figure 4 shows how CMC varies with distance, in which the coordinates of USVs are randomly generated. It can be observed that CMC decreases as the distance between USVs increases.

Table 2. Simulation parameter settings for figures.

Figure	v_{wind} (m/s)	H_{UAV} (m)	M_T	M_R	f_c (GHz)	Antenna Array
Figure 4	5	25	2	2	2.5	ULA
Figure 5	5	-	2	2	2.5	ULA
Figure 6	-	25	2	2	2.5	ULA
Figure 7	5	35	-	2	2.5	ULA
Figure 8	5	-	2	2	2.5	ULA
Figure 9	5	35	-	2	2.5	ULA
Figure 10	2	20	1	1	-	ULA
Figure 11	2	25	1	-	2.5	-
Figure 12	2	25	1	-	-	ULA
Figure 14	2	20	1	1	3.5	ULA
Figure 15	5	30	-	2	2.5	ULA

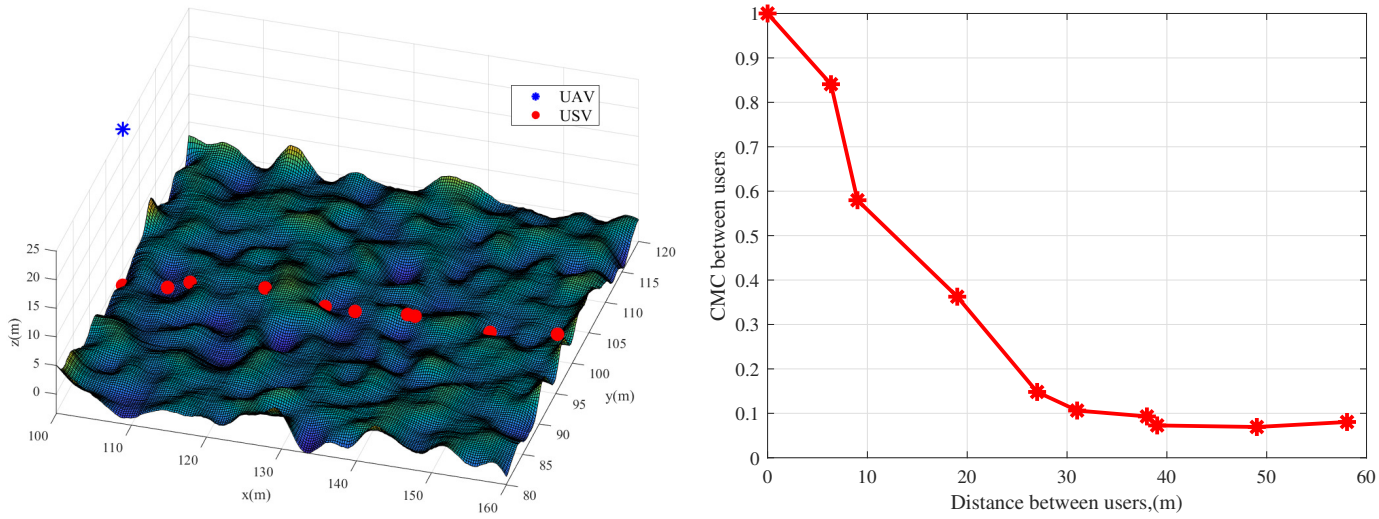

(**a**) (**b**)

Figure 4. (**a**) The positional schematic of the UAV and USVs; (**b**) the relationship between CMC and the distance between USVs in this scenario.

Figure 5 illustrates the impact of UAV flight heights on the channel correlation between USVs. It can be observed that regardless of the UAV flight height, the CMC value decreases as the distance between USVs increases and eventually approaches zero. Moreover, the increase in UAV flight height slows down the rate of CMC decline. This is because at higher height, the multipath parameters of different USVs gradually become similar. It leads to

similar signal attenuation and delay characteristics across different channels, and finally increases the similarity between channels.

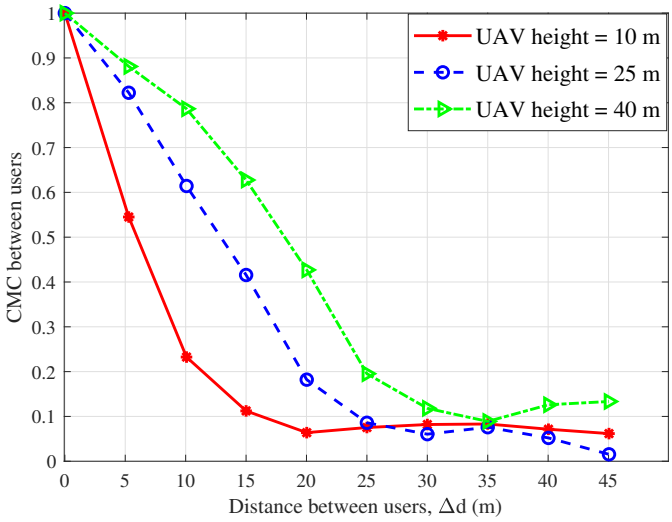

Figure 5. CMC at different UAV flight heights.

Figure 6 demonstrates the impact of wind speed on the CMC between USVs. It can be observed that the rate of CMC decline increases with higher wind speed. However, when the wind speed is 15 m/s and 20 m/s, the CMC curve exhibits noticeable peaks at certain distance points, followed by a subsequent drop. This phenomenon occurs because higher wind speed intensifies sea surface fluctuation. This leads to greater differences in distribution between the heights of USVs and sea surface clusters. This change increases the disparity in multipath parameters between different USVs, thus enhancing the randomness of the channel and finally accelerating the rate of CMC decline. At higher wind speeds, the amplitude of waves at certain locations becomes very large. This offsets the CMC reduction caused by the increased distance between the UAV and USV effectively. As a result, peaks appear at specific distance points in the CMC curve.

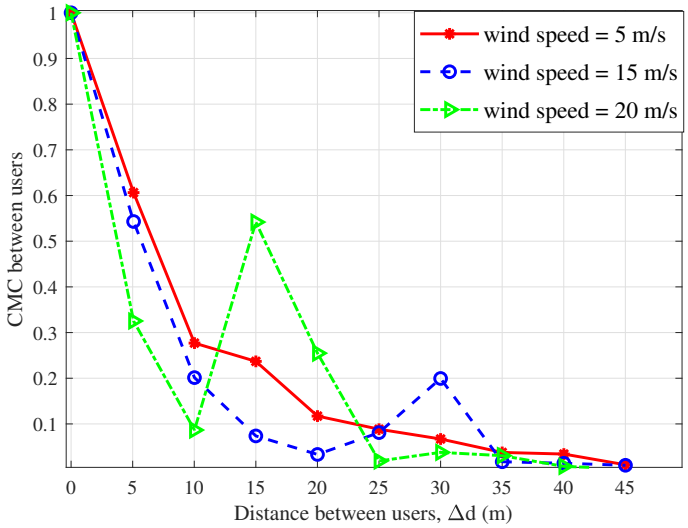

Figure 6. CMC at different wind speeds.

Figure 7 illustrates the impact of the number of transmitting antennas on CMC between USVs. It can be observed that as the number of antennas mounted on the UAV increases, the rate of CMC decline becomes faster. This phenomenon may be attributed to the fact that

an increase in the number of transmitting antennas leads to a greater number of channel paths received by the USV. As the diversity of channel paths increases, the multipath components between different USVs become more independent. This change expands the degrees of freedom of the channel and enhances the orthogonality of channels between different USVs, thereby reducing the channel correlation between them.

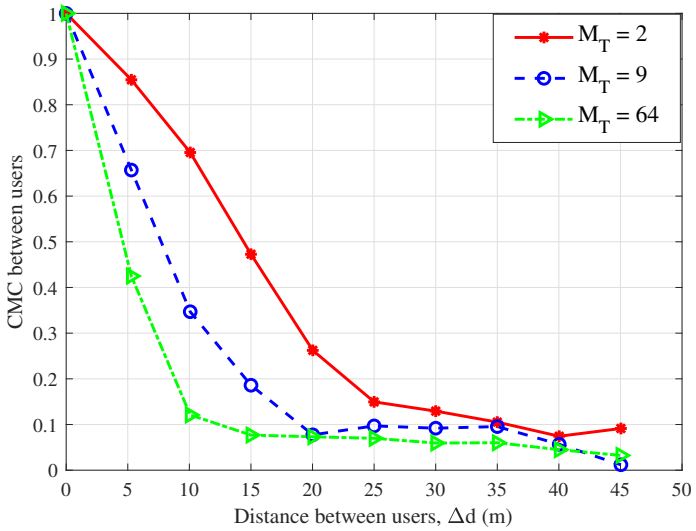

Figure 7. CMC at different numbers of transmitting antennas.

Figure 8 illustrates the impact of UAV flight heights on channel capacity of USVs. The simulation statistically analyzes the overall channel capacity of the USV group. From the figure, it can be observed that as the UAV flight height increases, the channel capacity gradually decreases. This phenomenon may be attributed to the increased distance between the transmitting and receiving antennas. It leads to greater signal attenuation and propagation delay [22]. The increased signal attenuation reduces the strength of received signals, thereby lowering the effective Signal-to-Noise Ratio (SNR) of the channel. Additionally, the increased propagation delay results in larger phase differences between multipath signals. This change further weakens the power of received signal. Consequently, these effects lead to a reduction in channel capacity.

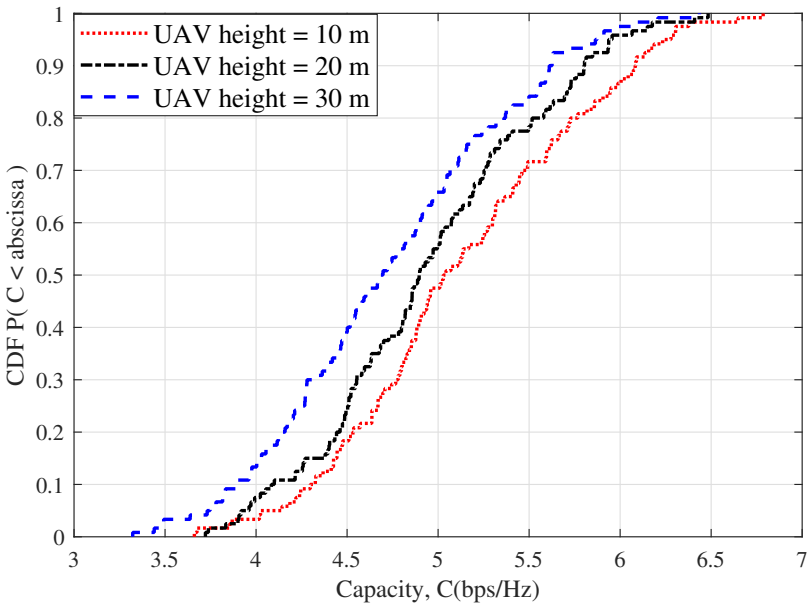

Figure 8. The CDFs of channel capacity at different UAV flight heights.

Figure 9 illustrates the impact of the number of transmitting antennas on the channel capacity of USVs. From the figure, it can be observed that as the number of transmitting antennas increases, the channel capacity exhibits an upward trend. This phenomenon may be attributed to the fact that, with the transmission power per antenna remaining constant, an increase in the number of transmitting antennas enables the USV to coherently combine multiple received signals, thereby improving the SNR. Additionally, the signal arriving at the USV through different paths helps mitigate multipath fading and reduces SNR fluctuations at USVs. Ultimately, these effects contribute to an increase in the channel capacity of USVs.

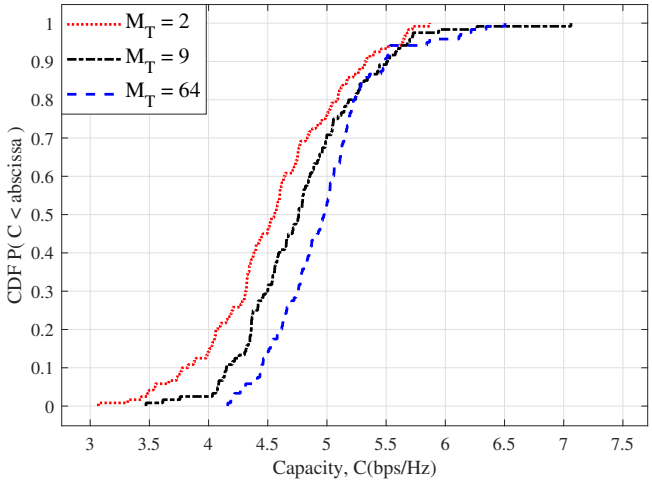

Figure 9. The CDFs of channel capacity at different numbers of transmitting antennas.

Figure 10 illustrates the impact of frequency bands and UAV speeds on the ACF of a single-link channel. The UAV trajectory is set as linear acceleration. From the figure, it can be observed that ACF exhibits a decreasing trend over time. Moreover, due to the linear increase in UAV speed, the UAV moves faster at the 1st second than at the 0th second, resulting in a more rapid decline in ACF. This indicates that an increase in UAV speed enhances the time-domain non-stationarity of the channel. Additionally, when the channel operates at a higher frequency band, the ACF declines even faster. This may be because an increase in operating frequency leads to greater signal phase shifts within the channel, thereby weakening the ACF.

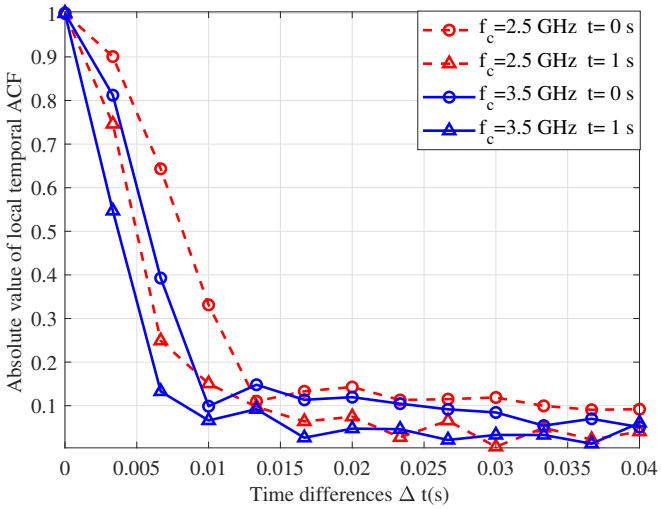

Figure 10. ACF at different frequency bands and time instants ($a_{\mathrm{UAV}} = 3\ \mathrm{m/s^2}$).

Figure 11 illustrates the impact of the MIMO antenna layouts and number of links on the CCF. From the figure, it can be observed that the CCF of the UCA layout declines significantly faster than the ULA layout. This phenomenon occurs because different antenna array layouts influence the emission angles (AAOD, EAOD) of an individual antenna. The ULA layout has a simple linear arrangement. Each antenna shares the same emission angle. In contrast, the UCA layout has a more complex arrangement, with each antenna having a different emission angle. This increases the channel differences between different antennas, and leads to a more rapid decrease in CCF as the antenna spacing increases. Furthermore, it can be observed that the descent rate of the CCF under multi-link conditions is significantly slower than that under single-link conditions. This indicates that the number of links in the communication model has a direct impact on the CCF.

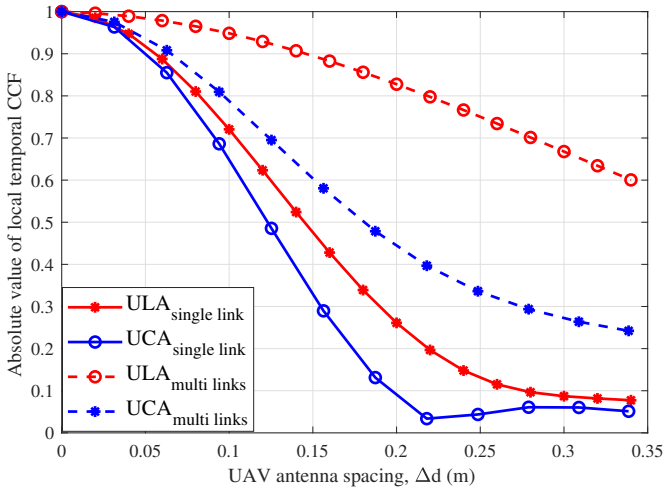

Figure 11. CCF at different MIMO antenna layouts and numbers of links.

Figure 12 illustrates the impact of frequency bands and antenna orientations on the CCF of a single-link channel. From the figure, it can be observed that as the frequency increases, the rate of CCF decline also accelerates. Additionally, the figure shows that a decrease in the antenna orientation of the UAV's transmitting antenna results in a lower CCF. This is because when the antenna of the UAV is directed toward the primary distribution region of the clusters, the channel becomes more sensitive to variations in the antenna position. It finally leads to a faster decline in CCF.

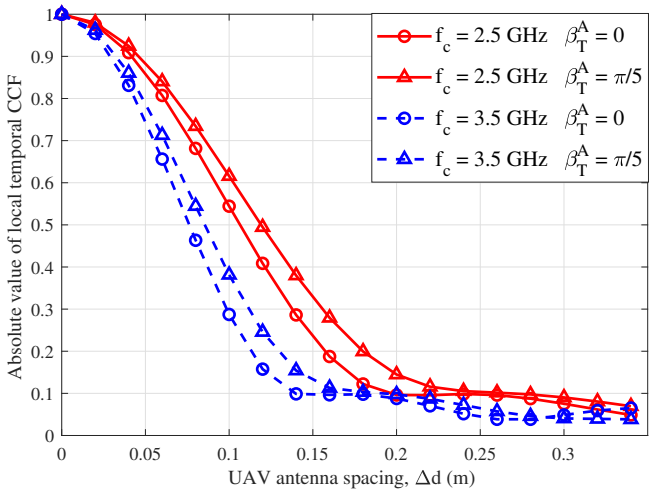

Figure 12. CCF at different frequency bands and antenna orientations.

Figure 13 illustrates the observation of scattering clusters by antennas in a ULA antenna layout. To clearly depict the birth and death of clusters, Figure 13a selectively displays the observation of the first four clusters by all antennas. It can be observed that some clusters are not detected by the transmitting antennas. It means clusters may disappear in this channel model. Figure 13b shows the number of clusters observed by antennas within the array under different correlation distances. As shown in the figure, as the correlation distance between antennas decreases, the number of observable clusters also decreases. This is because a smaller correlation distance reduces the observable radii of both the UAV and USVs. This change makes it more difficult for the randomly generated clusters to be detected.

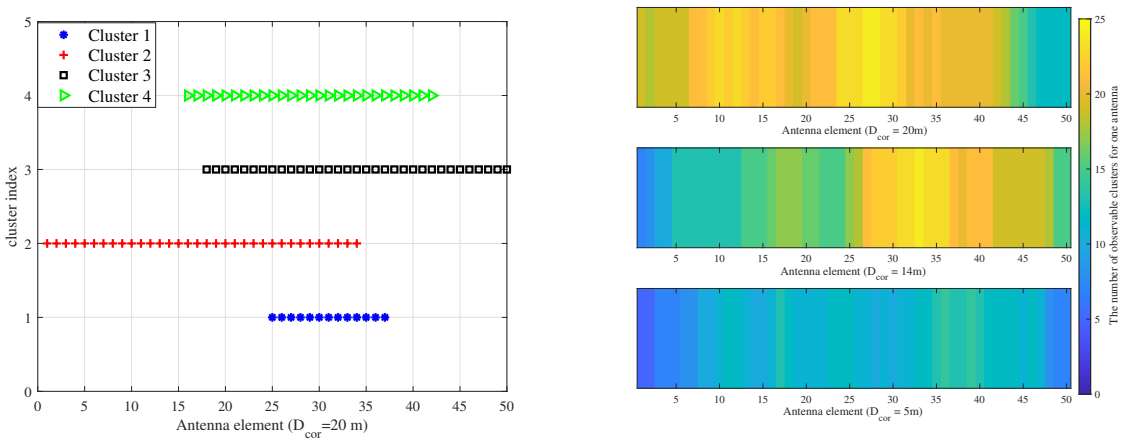

(**a**) (**b**)

Figure 13. Observation of clusters by transmitting antennas in a ULA layout; (**a**) Observation of specific clusters by the antenna array; (**b**) The number of clusters observed by the antenna within the array under different correlation distances.

5. Model Comparison and Analysis

To verify the authenticity and effectiveness of the proposed model, we conducted field channel measurements. The measurements were carried out near the coastline, where the ground receiver was positioned at the shore to emulate a stationary USV docked at the edge. During the measurement, the UAV flew at an altitude of 20 m, moving linearly away from the shore for a distance of 100 m at a speed of 5 m/s. The communication operated at a center frequency of 3.5 GHz. The measurement system consisted of airborne and ground components. The airborne unit comprised a Universal Software Radio Peripheral (USRP), an omnidirectional antenna, a microcomputer, and a compact power supply. The ground setup included a USRP, an omnidirectional antenna, a computer, and an outdoor power supply. Two USRPs and two omnidirectional antennas were employed for signal transmission and reception. During the measurement, high-order pseudo-noise (PN) sequences were transmitted from the Tx to the Rx. The simulation parameters are configured to match this scenario accordingly. The fitting results of RMS delay spread (RMS DS) and the auto-correlation function (ACF) under single-USV maritime scenarios are provided in Figure 14, which demonstrate the accuracy of the proposed model in single-link channel conditions.

To further validate the availability of the proposed model in multi-USV scenarios, we performed ray-tracing-based simulations in a reconstructed maritime environment as depicted in Figure 15a, and obtained the channel data employing ray-tracing techniques in a UAV-to-multi-USV communication setting. Based on the acquired channel data, the CMC among different users was calculated, and then compared with the results derived from the proposed model under the same parameter configurations. As illustrated in Figure 15b, Comparison Group 1

corresponds to a scenario where the UAV operates at an altitude of 30 m with a 3 × 3 transmit antenna array. Comparison Group 2 involves the same UAV altitude but utilizes an 8 × 8 transmit antenna array. The fitting results confirm the applicability and accuracy of the proposed model in UAV-to-multi-USV communication scenarios.

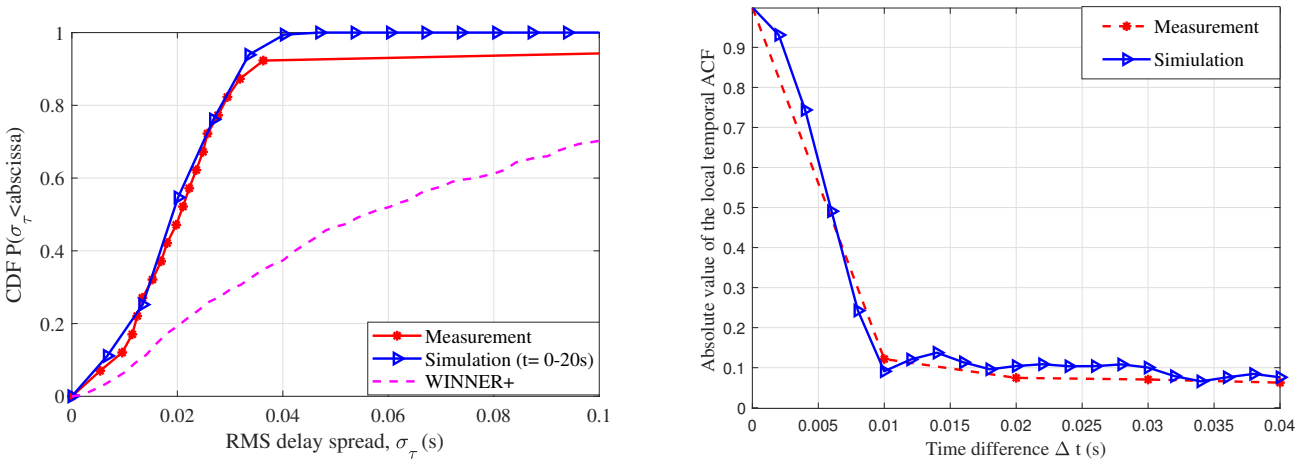

(**a**) (**b**)

Figure 14. (**a**) The CDF of the RMS DS with simulation and measurement data; (**b**) the ACF of the channel with simulation and measurement data ($v_{\mathrm{UAV}} = 5$ m/s, $v_{\mathrm{USV}} = 0.1$ m/s).

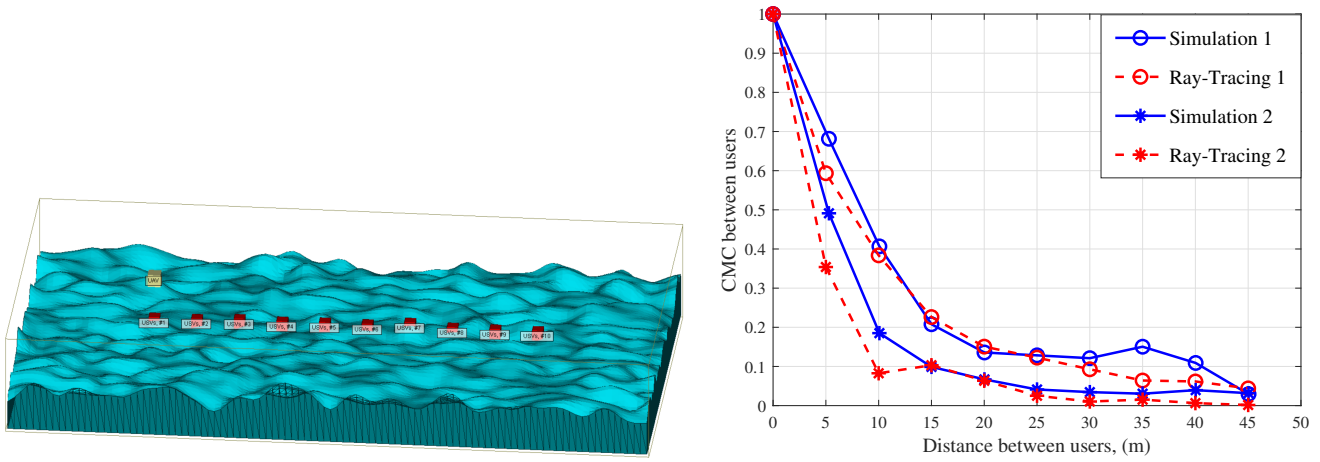

(**a**) (**b**)

Figure 15. (**a**) Ray-Tracing Scenario Reconstruction; (**b**) Comparison of the CMC obtained from Ray-Tracing and the proposed model.

6. Conclusions

In this paper, a novel channel model for maritime UAV-to-multi-USV communication has been proposed. This model incorporated a multi-USV receiving scenario within a maritime environment. To more realistically mimic the maritime UAV-to-multi-USV communication scenario, the observability of clusters in both the time and space domains was taken into account. Furthermore, the impacts of sea wave fluctuations and the waveguide effect were comprehensively considered and elaborated upon. Based on the proposed model, the key statistical properties of the channel model have also been studied, including the inter-USV CMC, channel capacity, temporal ACF and spatial CCF. The results have demonstrated that UAV flight height, wind speed, and the number of transmitting antennas significantly impact the CMC. Regarding channel capacity, the UAV flight height and the number of transmitting antennas influence the signal fading and multipath effects, thereby

affecting channel capacity. For a single-link channel, the results have revealed that temporal ACF decreases more rapidly with increasing operating frequency and UAV velocity. Additionally, this study has examined the impact of antenna layouts, number of links, operating frequencies, and antenna orientations on spatial CCF, and has presented a visualization of cluster observability. The results have shown that reducing the correlation distance between transmitting antennas decreases the observable radii, and finally makes randomly generated clusters less likely to be detected. Finally, the proposed channel model has been validated by comparing the simulation results with the measured data, demonstrating its effectiveness and accuracy under a single-link environment. In addition, the model's accuracy in multi-link environments is verified by comparing the CMC derived from the ray-tracing method with that obtained from the proposed model. In future research, we will prioritize channel measurements in maritime environments under multi-USV and multi-antenna configurations to further validate and refine the proposed model.

Author Contributions: Conceptualization, Y.L.; methodology, Y.L.; software, Y.Z. (Yuyang Zhang), Y.Z. (Yi Zhang) and J.H.; validation, Y.Z. (Yuyang Zhang), Y.Z. (Yi Zhang) and Y.L.; formal analysis, Y.Z. (Yuyang Zhang), Y.Z. (Yi Zhang) and Y.L.; investigation, Y.Z. (Yuyang Zhang), Y.Z. (Yi Zhang) and J.L.; resources, Y.L.; data curation, Y.L.; writing—original draft preparation, Y.Z. (Yuyang Zhang); writing—review and editing, Y.Z. (Yuyang Zhang), Y.Z. (Yi Zhang), J.L., B.H., H.C., Y.L. and J.H.; funding acquisition, Y.L. All authors have read and agreed to the published version of the manuscript.

Funding: This work was supported by the National Natural Science Foundation of China (NSFC) under Grants 62471279, 62271147 and 62301365, the Natural Science Foundation of Shandong Province under Grant ZR2024MF062, the Future Plan Program for Young Scholars of Shandong University, the Innovation and Technology Support Program for Young Scholars of Colleges and Universities in Shandong Province under Grant 2022KJ009, and the open research fund of the National Mobile Communications Research Laboratory, Southeast University, under Grant 2025D03.

Data Availability Statement: Data will be available upon request to the corresponding author.

Conflicts of Interest: The authors declare no conflicts of interest.

References

1. Nomikos, N.; Gkonis, P.K.; Bithas, P.S.; Trakadas, P. A survey on UAV-aided maritime communications: Deployment considerations, applications, and future challenges. *IEEE Open J. Commun. Soc.* **2022**, *4*, 56–78. [CrossRef]
2. Akhtar, M.W.; Saeed, N. UAVs-enabled maritime communications: UAVs-enabled maritime communications: Opportunities and challenges. *IEEE Syst. Man Cybern. Mag.* **2023**, *9*, 2–8. [CrossRef]
3. Yan, C.; Fu, L.; Zhang, J.; Wang, J. A comprehensive survey on UAV communication channel modeling. *IEEE Access* **2019**, *7*, 107769–107792. [CrossRef]
4. Kim, H.; Mokdad, L.; Ben-Othman, J. Designing UAV surveillance frameworks for smart city and extensive ocean with differential perspectives. *IEEE Commun. Mag.* **2018**, *56*, 98–104. [CrossRef]
5. Jiang, H.; He, R.; Ruan, C.; Zhou, J.; Chang, D. Three-dimensional geometry-based stochastic channel modeling for intelligent reflecting surface-assisted UAV MIMO communications. *IEEE Wirel. Commun. Lett.* **2021**, *10*, 2727–2731. [CrossRef]
6. Huang, Y.; Wu, Q.; Lu, R.; Peng, X.; Zhang, R. Massive MIMO for cellular-connected UAV: Challenges and promising solutions. *IEEE Commun. Mag.* **2021**, *59*, 84–90. [CrossRef]
7. Wang, W.; Jost, T.; Raulefs, R.; Fiebig, U.C. Ship-to-ship broadband channel measurement at 5.2 GHz on north sea. In Proceedings of the 2017 11th European Conference on Antennas and Propagation (EUCAP), Paris, France, 19–24 March 2017; pp. 3872–3876.
8. Sandra, M.; Tian, G.; Fedorov, A.; Cai, X.; Johansson, A.J. Measurement-based wideband maritime channel characterization. In Proceedings of the 2023 17th European Conference on Antennas and Propagation (EuCAP), Florence, Italy, 26–31 March 2023; pp. 1–4.
9. Li, C.; Yu, J.; Xue, J.; Chen, W.; Wang, S.; Yang, K. Maritime broadband communication: Wireless channel measurement and characteristic analysis for offshore waters. *J. Mar. Sci. Eng.* **2021**, *9*, 783. [CrossRef]
10. Reyes-Guerrero, J.C. Experimental broadband channel characterization in a sea port environment at 5.8 GHz. *IEEE J. Ocean. Eng.* **2015**, *41*, 509–514. [CrossRef]

11. Yang, C.; Wang, J.; Ma, J. Exploration of X-band communication for maritime applications in the South China Sea. *IEEE Antennas Wirel. Propag. Lett.* **2021**, *21*, 481–485. [CrossRef]
12. Álvarez, P.R.; Copa, A.J.N.; Cuiñas, I. Propagation over the sea between ship and UAV. In Proceedings of the 2020 IEEE International Symposium on Antennas and Propagation and North American Radio Science Meeting, Montreal, QC, Canada, 5–10 July 2020; pp. 1103–1104.
13. Ding, R.; Wang, J.; Li, Y.; You, L.; Sun, Q. A stochastic ray-tracing approach for maritime line-of-sight channel modeling. In Proceedings of the 2019 IEEE 19th International Conference on Communication Technology (ICCT), Xi'an, China, 16–19 October 2019; pp. 135–139.
14. Zheng, Y.; Yang, Y.; Wang, C.X.; Huang, J.; Feng, R. A Novel Ultra-Massive MIMO Beam Domain Channel Model for 6G Maritime Communications. In Proceedings of the GLOBECOM 2023-2023 IEEE Global Communications Conference, Kuala Lumpur, Malaysia, 4–8 December 2023; pp. 715–720.
15. He, Y.; Wang, C.X.; Chang, H.; Huang, J.; Sun, J.; Zhang, W.; Aggoune, E.H.M. A novel 3D non-stationary maritime wireless channel model. *IEEE Trans. Commun.* **2021**, *70*, 2102–2116. [CrossRef]
16. Yu, Y.; Rodríguez-Piñeiro, J.; Shunqin, X.; Tong, Y.; Zhang, J.; Yin, X. Measurement-based propagation channel modeling for communication between a UAV and a USV. In Proceedings of the 2022 16th European Conference on Antennas and Propagation (EuCAP), Madrid, Spain, 27 March–1 April 2022; pp. 1–5.
17. Chang, H.; Wang, C.X.; He, Y.; Bai, Z.; Sun, J.; Zhang, W. Multi-user UAV channel modeling with massive MIMO configuration. In Proceedings of the 2021 IEEE 94th Vehicular Technology Conference (VTC2021-Fall), Norman, OK, USA, 27–30 September 2021; pp. 1–6.
18. Su, P.; Chang, H.; Wang, C.X.; Ma, Y.; Huang, J.; He, Y. A Maritime Multi-User GBSM for Land-to-Ship Communications. In Proceedings of the 2024 IEEE 99th Vehicular Technology Conference (VTC2024-Spring), Singapore, 24–27 June 2024; pp. 1–6.
19. Miyamoto, K.; Nishibe, K.; Shibakura, T.; Tamura, K.; Cho, J.; Cho, S.; Cha, J.; Ahn, C.J. Analysis of MRT Precoding Massive MIMO for Railway & Maritime Terminal in Multi-cell Environment. *J. Electr. Eng. Technol.* **2025**, *20*, 855–860.
20. Tang, M.; Lau, V.K. Online Learning Algorithms for Zero-Sum Games of Linear Systems over Wireless MIMO Fading Channels with Uncountable State Space. In Proceedings of the 2023 62nd IEEE Conference on Decision and Control (CDC), Singapore, 13–15 December 2023; pp. 8751–8756.
21. Tang, M.; Cai, S.; Lau, V.K. Online System Identification and Optimal Control for Mission-Critical IoT Systems Over MIMO Fading Channels. *IEEE Internet Things J.* **2022**, *9*, 21157–21173. [CrossRef]
22. Diago-Mosquera, M.E.; Aragón-Zavala, A.; Rodriguez, M. Towards practical path loss predictions in indoor corridors considering 5G mmWave three-dimensional measurements. *IEEE Antennas Wirel. Propag. Lett.* **2022**, *21*, 2055–2059. [CrossRef]

Disclaimer/Publisher's Note: The statements, opinions and data contained in all publications are solely those of the individual author(s) and contributor(s) and not of MDPI and/or the editor(s). MDPI and/or the editor(s) disclaim responsibility for any injury to people or property resulting from any ideas, methods, instructions or products referred to in the content.